Supplemental Material to: Enhanced Third-Order Optical Nonlinearity Driven by Surface-Plasmon Field Gradients

Vasily Kravtsov,[1] Sultan AlMutairi,[2] Ronald Ulbricht,[1] A. Ryan Kutayiah,[2] Alexey Belyanin,[2] and Markus B. Raschke[1,*]

[1]*Department of Physics, Department of Chemistry, and JILA, University of Colorado, Boulder, CO, 80309, USA*

[2]*Department of Physics and Astronomy, Texas A&M University, College Station, TX, 77843, USA*

(Dated: April 29, 2018)

* Corresponding authors: belyanin@physics.tamu.edu, markus.raschke@colorado.edu

I. Incoherent Emission

The four-wave mixing spectral peak observed in this work typically appears superimposed on a broad incoherent emission background. The exact mechanism of this emission is currently under debate, and can involve radiative recombination of laser-excited hot electrons within the conduction band [1, 2] or fast electronic Raman processes [3, 4]. In both cases, the emission process involves electronic transitions within the *sp*-band of Au, which require additional momentum. The emission is therefore strongly enhanced in nanostructures where the momentum is provided through near-field modes as discussed in the main text.

The spectrum of the incoherent emission depends on the temperature of the electron gas through the Fermi–Dirac distribution of the electronic occupation numbers, and can empirically be approximated by a Boltzmann distribution. The power dependence of the emission intensity therefore varies with wavelength. Fig. S1a shows power law fits for the incoherent emission intensity vs. excitation power for 3 different wavelength in the emission spectrum: $\lambda_1 = 660$ nm (black), $\lambda_2 = 710$ nm (red), and $\lambda_3 = 770$ nm (blue). The extracted power law exponent varies from 1.50 ± 0.16 to 2.59 ± 0.02 in the selected range. The full spectral dependence of the power law exponent is shown in (b), with extracted data (gray) and average as a guide to the eye (red).

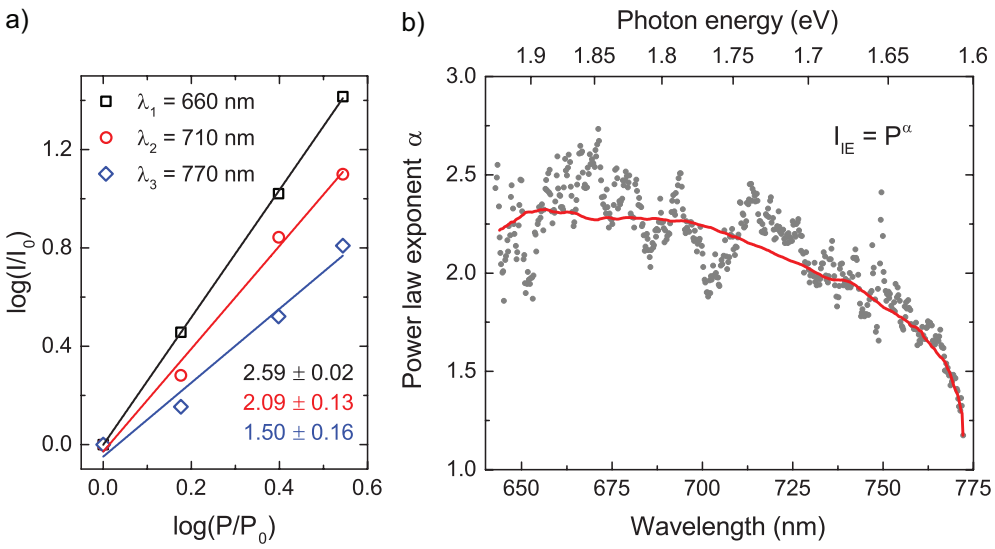

Fig. S1. (a) Power dependence of the spectral intensity of the incoherent emission from tip apex for three selected wavelength values of 660 nm (black), 710 nm (red), and 770 nm (blue), together with power law fits (lines) on a log-log plot. (b) Wavelength dependence of power law exponent extracted from fitting the incoherent emission.

II. FWM Measurements on Rod-Shaped Au Nano-Antennas

In order to show that our conclusions on the FWM mechanism are not limited to conical tips but apply to any metallic nano-structure of different geometries, we performed FWM measurements on Au nano-rods as shown schematically in Fig. S2a. The nano-structures are assembled into periodic arrays to increase signal levels and avoid heat-induced damage in the case of single-particle spectroscopy. The dimensions of the nano-particles are designed to support localized plasmon resonance at the excitation wavelength, in order to increase the FWM response through local field enhancement.

Periodic arrays of nano-rods are fabricated on glass substrates by e-beam lithography, with subsequent deposition of a Ti adhesion and Au layers followed by lift-off. Ensemble-averaged extinction spectra are taken in transmission geometry and shown in Fig. S2b for two samples with plasmon resonances centered around 800 nm (Array 1, black) and 730 nm (Array 2, blue). The samples are illuminated through a microscope objective by shaped Ti:Sapphire laser pulses containing two narrow bands with frequencies ω_1 and ω_2. The focal spot size is designed to cover ~ 100 nano-particles. An ensemble-averaged FWM signal is collected in the back-scattering geometry through the same objective.

For the case of plasmon-resonant nano-rods, the experimental FWM efficiency η'_{FWM} will include frequency-dependent local field enhancement factors L at frequencies ω_2 and $\omega_{\mathrm{FWM}} = 2\omega_1 - \omega_2$:

$$\eta'_{\mathrm{FWM}} \propto \left[\chi^{(3)}\right]^2 \cdot L^2(\omega_2) \cdot L^2(\omega_{\mathrm{FWM}}). \tag{1}$$

Assuming the extinction spectrum $A(\omega)$ to be also proportional to $L^2(\omega)$, we can normalize the experimental FWM efficiency such that it only includes the third-order susceptibility,

$$\eta_{\mathrm{FWM}} = \frac{\eta'_{\mathrm{FWM}}}{A(\omega_2) \cdot A(2\omega_1 - \omega_2)} \propto \left[\chi^{(3)}\right]^2, \tag{2}$$

where the extinction data from Fig. S2b is used to obtain $A(\omega)$.

The results for samples 1 and 2 are shown in Fig. S2c-d and exhibit the same general trend as the results presented in the main text for the case of a single non-resonant tip. We note that the FWM measurements on the nano-rods are ensemble-averaged, with possible inhomogeneous broadening.

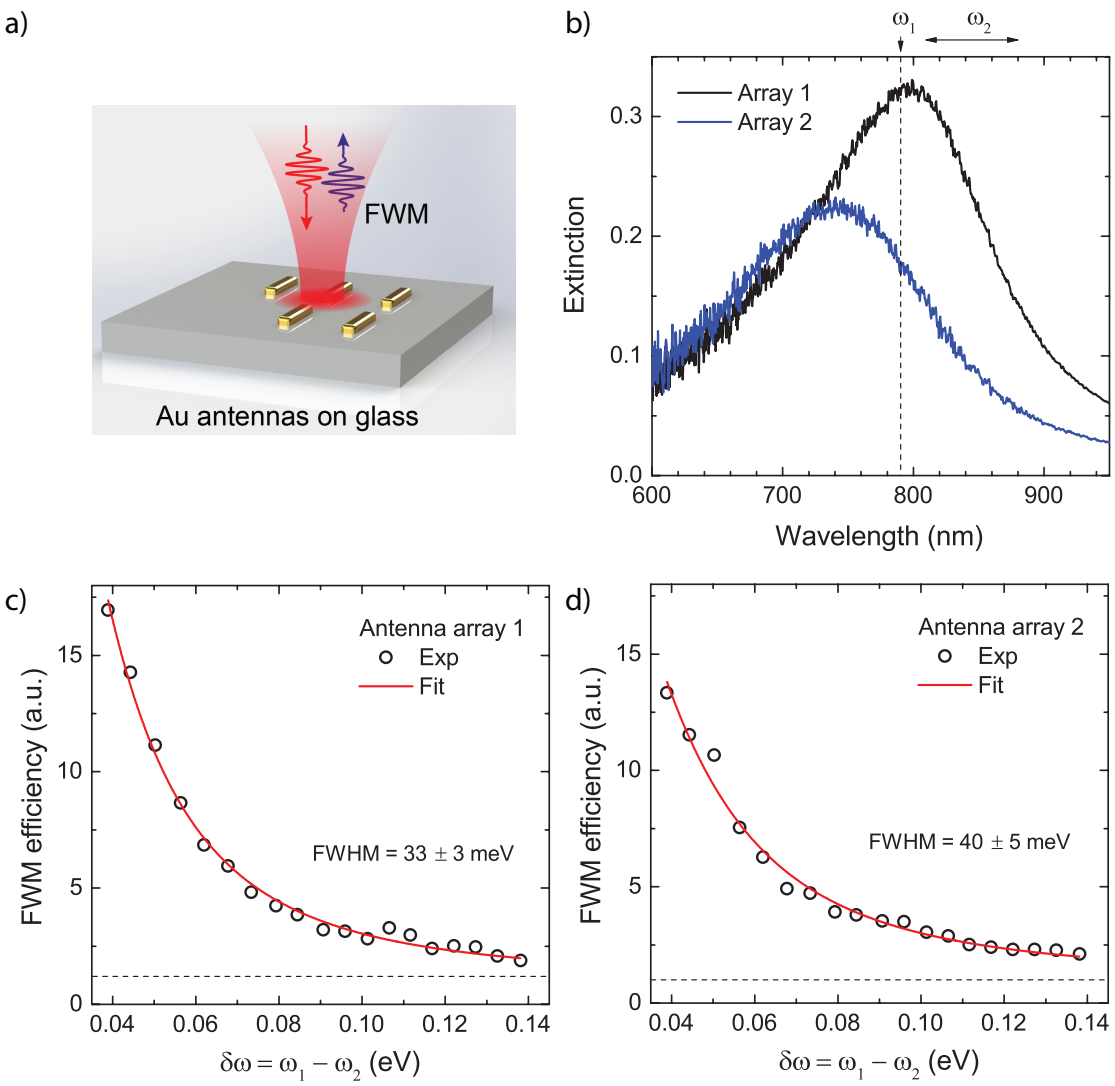

Fig. S2. (a) Schematic of the FWM measurement on rod-shaped Au nano-antennas: sample containing a periodic array of antennas fabricated on glass is illuminated in far-field by Ti:Sapphire pulses with frequencies ω_1, ω_2, and a FWM response is detected in the back-scattering geometry. (b) Extinction spectra measured on two antenna arrays designed for different plasmon resonance condition. (c)-(d) Resulting FWM efficiency as a function of the detuning between ω_1 and ω_2 for the two antenna arrays (black circles) together with Lorentzian fits (red curves).

III. FWM Measurements on Different Tips

In the main text, the FWM data are shown for a single tip. In order to explore the variation of FWM efficiency due to changes in tip geometry, we measure FWM detuning dependences on multiple different tips. Fig. S3a shows experimental FWM efficiency spectra for three selected tips that

exhibit significantly different strength of nonlinear response and different apex radii as observed with scanning electron microscopy. As can be seen in the figure, all three FWM efficiency spectra are well fit by Lorentzian functions, with similar full width at half maximum (fwhm), while the amplitudes of the Lorentzians vary from 2.2 for Tip C to 8.7 for Tip A. In our model, the amplitude of the Lorentzian is equal to the ratio of the intraband term in the third-order nonlinear susceptibility at zero detuning $\chi^{(3)}_{\text{intra}}(0)$ to the third-order nonlinear susceptibility of Au $\chi^{(3)}_{\text{Au}}$. Further, this ratio depends on the radius of curvature of the nano-particle as $\chi^{(3)}_{\text{intra}}(0)/\chi^{(3)}_{\text{Au}} \propto 1/R^2$. Therefore, the different Lorentzian amplitudes extracted for different tips correspond to the varying tip apex radii. We note that, as the tip geometry deviates from that of an ideal sphere assumed in the model, the variations in the tip shape, such as the apical angle, will effectively appear as variations in the radius of curvature extracted from the Lorentzian fit.

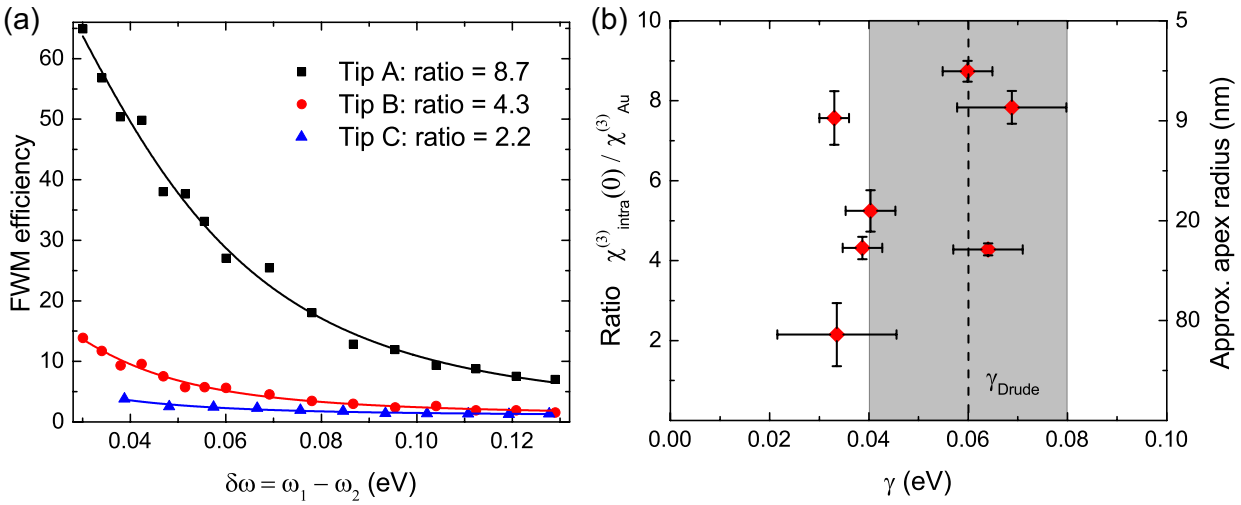

Fig. S3. (a) FWM efficiency as a function of detuning measured for tips of different sharpness. The difference in the relative contribution of the intraband third-order nonlinearity can be clearly observed as the change in the FWM efficiency at zero detuning. (b) Parameters extracted from experimental data for different tips and antennas used in the experiment: the linewidth of the Lorentzian fit, corresponding to the electron collision rate (x-axis), and the amplitude of the Lorentzian fit, corresponding to the relative contribution of the intraband nonlinearity term (y-axis). The radii on the right axis are given approximately based on the distribution of tip apex sizes used in the experiment and the $1/R^2$ scaling of the Lorentzian amplitude in the model. Gray shaded region indicates the range of Drude relaxation rates γ_{Drude} reported in literature.

Fig. S3b summarizes the parameters extracted from the Lorentzian fitting of FWM curves for

a number of tips. As can be seen in the figure, the range of electron collision rates γ (x-axis) is in agreement with the Drude relaxation rate within experimental error. The variation in intraband to interband contributions (y-axis) shows no correlation with γ, in general agreement with our model. Here, γ as the electron collision rate is independent of the tip geometry for our range of tip radii, while the Lorentzian amplitude scales with the radius of curvature as $1/R^2$. This confirms the validity of our model and demonstrates how the FWM efficiency curves vary with varying shape and size of nano-tips.

IV. Spectral Filtering Effects

In general, the presence of the grating on the tip shaft can result in various spectral filtering effects that make the SPP spectrum at the tip apex deviate from that of the laser light incident onto the grating. In our case, these effects have a broadband character, which is due to the following reasons. First, we use a fan-shaped grating, where, within the focal spot of the incident laser beam, the period of the grating is slightly different, resulting in splitting and filtering of different frequencies. Second, the incident light on the grating is slightly defocused, with a distribution of incident angles, resulting in a similar spectral broadening effect. Finally, the laser beam incident onto the grating is usually coupled into SPPs closer to the lower end of the grating, so that the propagation of SPPs through the grating and associated spectral splitting effects are minimized. Most importantly, while any change in the spectral intensity of the SPPs propagating on the tip will result in a corresponding change in the FWM efficiency, in our experiment, the FWM data is normalized by a reference value calculated based on the SPP spectrum at the tip apex. Therefore, any effects related to the spectral filtering and splitting introduced by the grating should cancel out during this normalization, leaving our FWM efficiency results unaffected.

V. Model

Consider the situation when all fields participating in FWM have frequencies significantly below the interband transition edge in gold. In this case, as we show below, the FWM signal can be dominated by the intraband response of free-carrier plasma, even if electrons in gold are assumed to have a parabolic dispersion. The dominant component of the third-order current $\mathbf{j} = en^{(0)}\mathbf{v}^{(3)}$ is purely longitudinal, i.e. it is generated by FWM of longitudinal electric fields of the plasmon modes. The nanotip or nanoparticle geometry facilitates outcoupling of the longitudinal current oscillations to the outgoing transverse EM waves.

Neglecting the thermal motion, the equation of motion for a degenerate electron plasma against the neutralizing background of immobile ions is

$$\frac{\partial \mathbf{v}}{\partial t} + \frac{\mathbf{v}}{\tau} + (\mathbf{v}\cdot\nabla)\,\mathbf{v} - \frac{e}{m_e}\mathbf{E} - \frac{e}{m_e c}\mathbf{v}\times\mathbf{B} = 0. \tag{3}$$

with external electric and magnetic fields $\mathbf{E}$ and $\mathbf{B}$, electron velocity $\mathbf{v}$, effective mass m_e, electron charge e, and mean free time between electron collisions τ. Eq. 3 has to be supplemented with the continuity equation. However, we will need only the zeroth-order (unperturbed) electron density.

We assume that the electric fields of all modes, the field gradients, and the electron velocity perturbation are along x axis, $\mathbf{E} = E\hat{x}$ and $\mathbf{v} = \mathrm{v}\hat{x}$. We also neglect the contribution from the magnetic field. Then Eq. (1) reduces to

$$\frac{\partial \mathrm{v}}{\partial t} + \frac{\mathrm{v}}{\tau} + \mathrm{v}\frac{\partial \mathrm{v}}{\partial x} - \frac{e}{m_e}E = 0 \tag{4}$$

We seek a solution to Eq. (2) in the form of a perturbation expansion

$$\mathrm{v} = \lambda \mathrm{v}^{(1)} + \lambda^2 \mathrm{v}^{(2)} + \lambda^3 \mathrm{v}^{(3)} + \cdots$$

and write the field as $E = \sum_n E_n e^{-i\omega_n t}$ where ω_n take the values $\pm\omega_1$, $\pm\omega_2$ etc., and E_n take the values E_1, E_2, ... for positive frequencies and E_1^*, E_2^*, ... for negative frequencies.

We obtain the following set of equations

$$\frac{\partial \mathrm{v}^{(1)}}{\partial t} + \frac{\mathrm{v}^{(1)}}{\tau} = \frac{e}{m_e}\sum_n E_n e^{-i\omega_n t}, \tag{5}$$

$$\frac{\partial \mathrm{v}^{(2)}}{\partial t} + \frac{\mathrm{v}^{(2)}}{\tau} + \mathrm{v}^{(1)}\frac{\partial \mathrm{v}^{(1)}}{\partial x} = 0, \tag{6}$$

$$\frac{\partial \mathrm{v}^{(3)}}{\partial t} + \frac{\mathrm{v}^{(3)}}{\tau} + \mathrm{v}^{(1)}\frac{\partial \mathrm{v}^{(2)}}{\partial x} + \mathrm{v}^{(2)}\frac{\partial \mathrm{v}^{(1)}}{\partial x} = 0. \tag{7}$$

The linear perturbation from Eq. (3) is

$$\mathrm{v}^{(1)}(t) = \frac{e}{m_e}\sum_n \frac{E_n e^{-i\omega_n t}}{\gamma - i\omega_n}, \tag{8}$$

where $\gamma = 1/\tau$.

We will be interested in the response at frequency $\omega_3 = 2\omega_1 - \omega_2$ to the two pump fields at frequencies ω_1 and ω_2. For small detunings $\omega_1 - \omega_2$ the main contribution comes from the second-order perturbation $\mathrm{v}^{(2)}$ at the beatnote frequency $\sim e^{-i(\omega_1-\omega_2)t}$. However, we will keep all the terms until the final expression is obtained. Then Eq. (4) becomes

$$\frac{\partial \mathrm{v}^{(2)}}{\partial t} + \frac{\mathrm{v}^{(2)}}{\tau} = -\left(\frac{e}{m_e}\right)^2 \sum_{n,m} \frac{E_n \partial_x E_m e^{-i(\omega_n+\omega_m)t}}{(\gamma - i\omega_n)(\gamma - i\omega_m)}. \tag{9}$$

Its solution is

$$\mathrm{v}^{(2)}(t) = -\left(\frac{e}{m_e}\right)^2 \sum_{n,m} \frac{E_n \partial_x E_m e^{-i(\omega_n+\omega_m)t}}{(\gamma - i\omega_n)(\gamma - i\omega_m)(\gamma - i(\omega_n+\omega_m))}. \tag{10}$$

Substituting $\mathrm{v}^{(1)}$ and $\mathrm{v}^{(2)}$ into Eq. 7, we obtain

$$\begin{aligned}\frac{\partial \mathrm{v}^{(3)}}{\partial t} + \frac{\mathrm{v}^{(3)}}{\tau} = &\left(\frac{e}{m_e}\right)^3 \sum_{n,m,l} \frac{E_l \partial_x (E_n \partial_x E_m) e^{-i(\omega_n+\omega_m+\omega_l)t}}{(\gamma - i\omega_n)(\gamma - i\omega_m)(\gamma - i\omega_l)(\gamma - i(\omega_n+\omega_m))} + \\ &\left(\frac{e}{m_e}\right)^3 \sum_{n,m} \frac{E_n \partial_x E_m \partial_x E_l e^{-i(\omega_n+\omega_m+\omega_l)t}}{(\gamma - i\omega_n)(\gamma - i\omega_m)(\gamma - i\omega_l)(\gamma - i(\omega_n+\omega_m))}.\end{aligned} \tag{11}$$

To get a numerical estimate, we replace ∂_x with $1/R$ where R is the radius of the tip apex. This gives

$$\frac{\partial \mathrm{v}^{(3)}}{\partial t} + \frac{\mathrm{v}^{(3)}}{\tau} = \frac{3e^3}{m_e^3 R^2} \sum_{n,m,l} \frac{E_n E_m E_l e^{-i(\omega_n+\omega_m+\omega_l)t}}{(\gamma - i\omega_n)(\gamma - i\omega_m)(\gamma - i\omega_l)(\gamma - i(\omega_n+\omega_m))} \tag{12}$$

Integration gives

$$\mathrm{v}^{(3)} = \frac{3e^3}{m_e^3 R^2} \sum_{n,m,l} \frac{E_n E_m E_l e^{-i(\omega_n+\omega_m+\omega_l)t}}{(\gamma - i\omega_n)(\gamma - i\omega_m)(\gamma - i\omega_l)(\gamma - i(\omega_n+\omega_m))(\gamma - i(\omega_n+\omega_m+\omega_l))}. \tag{13}$$

Now we select only the response at $\omega_3 = \omega_n + \omega_m + \omega_l = 2\omega_1 - \omega_2$; moreover, we keep only the terms that have resonance when $\omega_1 - \omega_2 \to 0$, i.e. $n = l = 1$, $m = -2$ and $m = l = 1$, $n = -2$. This gives

$$\mathrm{v}^{(3)}(t) = \frac{3e^3}{m_e^3 R^2} \frac{E_1^2 E_2^* e^{-i\omega_3 t}}{(\gamma - i\omega_1)^2 (\gamma + i\omega_2)(\gamma - i\omega_3)} \left(\frac{1}{(\gamma - i(\omega_1 - \omega_2))} + \frac{1}{(\gamma + i(\omega_1 - \omega_2))}\right) \tag{14}$$

Using $P = \chi^{(3)} E_1^2 E_2^* e^{-i\omega_3 t}$ and $j = \dfrac{dP}{dt} = en^{(0)}\mathrm{v}^{(3)}$ we obtain

$$\chi^{(3)} = i\frac{6n^{(0)}e^4}{\omega_3 m_e^3 R^2}\frac{\gamma}{(\gamma - i\omega_1)^2(\gamma + i\omega_2)(\gamma - i\omega_3)\left(\gamma^2 + (\omega_1 - \omega_2)^2\right)}. \tag{15}$$

There is an obvious resonance at $\omega_1 = \omega_2$ with a Lorentzian FWHM equal to 2γ. For a numerical estimate, we assume all frequencies $\omega_{1,2,3} \sim 1.5$ eV and take $n^{(0)} = 6 \times 10^{22}$ cm^{-3}, m_e equal to the effective electron mass in Au, $2R = 15$ nm, and $\gamma = 64$ meV from the fit to the experimental FWM efficiency (frequencies have to be converted into s^{-1}). Then

$$|\chi^{(3)}| \sim \frac{6n^{(0)}e^4}{m_e^3 \gamma R^2 \omega_1^2 \omega_2 \omega_3^2} \sim 7.6 \times 10^{-12} \text{ esu}. \tag{16}$$

This corresponds to $|\chi^{(3)}| \sim 1.1 \times 10^{-19}$ m^2/V^2 in SI units.

---

[1] Haug, T., Klemm, P., Bange, S. & Lupton, J. M. Hot-electron intraband luminescence from single hot spots in noble-metal nanoparticle films. *Phys. Rev. Lett.* **115**, 067403 (2015).

[2] Lin, K. Q. *et al.* Intraband hot-electron photoluminescence from single silver nanorods. *ACS Photonics* **3**, 1248–1255 (2016).

[3] Hugall, J. T. & Baumberg, J. J. Demonstrating photoluminescence from Au is electronic inelastic light scattering of a plasmonic metal: the origin of SERS backgrounds. *Nano Lett.* **15**, 2600–2604 (2015).

[4] Mertens, J., Kleemann, M.-E., Chikkaraddy, R., Narang, P. & Baumberg, J. J. How light is emitted by plasmonic metals. *Nano Lett.* **17**, 2568–2574 (2017).